Nonharmonic contributions to the high-temperature phonon thermodynamics of Cr

C. M. Bernal-Choban,[1,*,†] H. L. Smith,[2,*,‡] C. N. Saunders,[1] D. S. Kim,[3] L. Mauger,[4] D. L. Abernathy,[5] and B. Fultz[1,§]

[1]*Applied Physics and Materials Science, California Institute of Technology, Pasadena, California 91125, USA*
[2]*Physics and Astronomy, Swarthmore College, Swarthmore, Pennsylvania 19081, USA*
[3]*Department of Materials Science and Engineering, Massachusetts Institute of Technology, Cambridge, Massachusetts 02139, USA*
[4]*Jet Propulsion Laboratory, Pasadena, California 91109, USA*
[5]*Neutron Scattering Division, Oak Ridge National Laboratory, Oak Ridge, Tennessee 37831, USA*

(Received 14 June 2022; revised 21 December 2022; accepted 15 February 2023; published 27 February 2023)

Phonon densities of states (DOSs) of body-centered cubic chromium were measured by time-of-flight inelastic neutron scattering at temperatures up to 1493 K. Density functional theory calculations with both quasiharmonic (QH) and anharmonic (AH) methods were performed at temperatures above the Néel temperature. Features in the phonon DOSs decrease in energy (soften) substantially with temperature. A Born–von Kármán analysis using fits to the experimental DOSs reveals a softening of almost 17% of the high-transverse phonon branch between 330 and 1493 K. The low-transverse branch changes by approximately half this amount. The AH calculations capture the observed behavior of the two transverse phonon branches, but the QH calculations give some inverted trends. Vibrational entropies from phonons and electrons are obtained, and their sum is in excellent agreement with the entropy of chromium obtained by calorimetry, indicating that above 330 K, no explicit temperature-dependent magnetic contributions are necessary.

DOI: 10.1103/PhysRevB.107.054312

I. INTRODUCTION

Understanding the vibrational, electronic, and magnetic interactions in condensed matter is fundamental to predicting the thermodynamic functions of materials such as free energy, internal energy, and entropy. These thermodynamic functions are essential for constructing phase diagrams, predicting thermal expansion, and explaining the temperature dependence of elastic constants, bulk moduli, and magnetization [1]. There are active investigations into these topics for their own sake, and for their importance to the structure and properties of materials [2–7].

One intriguing system is body-centered cubic (bcc) chromium, whose vibrational, electronic, and magnetic free energy contributions result in a transition from an antiferromagnet to a paramagnet, and show an apparent anharmonicity with increasing temperature [8]. Below the Néel transition temperature, $T_N = 311$ K, a single crystal of Cr is a conventional itinerant antiferromagnet [9]. At T_N, Cr retains the bcc structure but becomes paramagnetic [10,11]. In general, the free energy of Cr, F, requires three contributions to the entropy

$$F(M, V, T) = U - T(S_{\text{mag}} + S_{\text{ele}} + S_{\text{vib}}), \tag{1}$$

where M is magnetization, V is volume, T is temperature, U is the internal energy, S_{mag} is the magnetic entropy, S_{ele} is the electronic entropy, and S_{vib} is the vibrational entropy. The S_{vib} gives most of the total entropy at higher temperatures, even in a harmonic model with fixed phonon frequencies, $\{\omega_s\}$ [1]. Phonon frequencies change with volume, and the "quasiharmonic" (QH) approximation assumes that phonon frequencies, $\omega_s(V(T))$, depend on temperature only through thermal expansion. The "anharmonic" (AH) approximation includes an independent change with T, i.e., $\omega_s(V, T)$.

The lattice dynamics of Cr show large anharmonic contributions at high temperatures [8]. Transitions from the antiferromagnetic to the paramagnetic states are not well understood for Cr [12–16]. It has been suggested that magnetic fluctuations exist above 1000 K [15,17]. These issues of magnetism and anharmonicity continue to drive work on the high-temperature thermodynamics of Cr. Calorimetric (JANAF) measurements and third-generation CALPHAD models provide values for the total entropy of Cr, $S_{\text{tot}}(T)$ [18,19], but not the individual components of Eq. (1).

Here we use time-of-flight (TOF) inelastic neutron scattering (INS), Born–von Kármán (BvK) analyses, temperature-dependent effective potential modeling, and non-spin-polarized density functional theory (DFT) to determine the individual contributions S_{vib}, S_{ele}, and S_{mag}, from 330 to 1493 K. Our AH calculations, which include contributions from electrons and phonons, largely account for the values of $S_{\text{tot}}(T)$ observed with recent calorimetry measurements and match observed lattice expansion. The QH approximation also gives a vibrational entropy close to that observed with TOF INS, but this success is caused by a canceling effect of individual phonon branches. The BvK analyses of TOF data support AH phonon branch behavior. A comparison of TOF INS and anharmonic calculations reveals that AH computations capture most, but not all, experimentally observed phonon behavior. This additional

*These authors contributed equally to this work.
†cmbchoban@gmail.com
‡hsmith@swarthmore.edu
§btf@caltech.edu

nonharmonic behavior is unexplained but is not explicitly magnetic in origin. In summary, we find that temperature-broadened electronic and third-order anharmonic contributions reproduce experimental thermodynamic measurements well, and no purely magnetic interactions are needed to explain the thermodynamics of Cr above 330 K.

II. METHODS

A. Inelastic neutron scattering

Inelastic neutron scattering (INS) measurements were performed on electrochemically deposited plates of polycrystalline 99.995% Cr. Two pieces of Cr that gave a large area for scattering were secured inside a niobium foil sachet surrounded by a frame of boron nitride. All data were taken at the time-of-flight wide Angular-Range Chopper Spectrometer (ARCS) at the Spallation Neutron Source (SNS) at Oak Ridge National Laboratory (ORNL) [20]. The incident energy was 70 meV with the Fermi chopper at 420 Hz and the T_0 chopper at 90 Hz. Sample temperatures varied from 6–1493 K. Below 330 K, a closed-cycle helium refrigerator was used. For measurements at higher temperatures, samples were transferred to the high-temperature MICAS furnace [21].

Data were reduced to phonon density of states (DOS) curves by subtraction of an empty Nb sachet and were corrected for multiphonon scattering with Mantid and the Multiphonon package [22,23]. Integration to produce the phonon density of states was performed for values of 3.5 $\text{Å}^{-1} < Q < 10\ \text{Å}^{-1}$, where magnetic scattering contributes less than 1.5% of the total scattering. This ensured that the scattering intensity used to obtain the density of states was vibrational in origin. Additional corrections to account for sample curvature were performed in MCViNE [24] (see Supplemental Material [25] for more details).

B. Born–von Kármán analysis

Analyses of TOF INS DOSs were performed using the Born–von Kármán (BvK) model [26]. This model takes a crystal to be a set of nuclear masses whose interactions act like springs that provide restoring forces against the displacements of nuclei. By transforming the forces associated with these displacements into a dynamical matrix, the BvK model has often been used to fit phonon dispersions. Fitting phonon DOS spectra with the BvK model is more involved because the DOSs are aggregates of all phonon modes in reciprocal space. To address this challenge, trial force constants were used to construct a dynamical matrix, $D(\vec{q})$, using the underlying symmetries of the crystal lattice. A sufficiently dense set of q points in the first Brillouin zone was used to collect the spectrum of phonon frequencies, ω, for each temperature:

$$M\omega^2\vec{\epsilon} = D(\vec{q})\vec{\epsilon}, \tag{2}$$

where M is the mass of the atom and $\vec{\epsilon}$ is the polarization of the phonon mode corresponding to reciprocal space vector $\vec{q}$. This BvK model was embedded in a genetic algorithm global optimization framework, where trial sets of force constants were generated randomly according to the differential evolution algorithm [27]. Each optimization was repeated several times to ensure convergence. The resulting DOSs are compared with experimental data. For Cr, a BvK model including atomic interactions through the second nearest neighbors (four tensorial force constants) was found to be sufficient. More details of the fitting process are in the Supplemental Material [25].

C. Computation

All density functional theory (DFT) calculations were performed with the Vienna *Ab Initio* Simulation Package (VASP) [28–30]. Plane-wave basis sets with a kinetic energy cutoff of 600 eV and projector-augmented-wave pseudopotentials [31,32] were used with Perdew-Burke-Ernzerhof (PBE) exchange-correlation functionals [33,34]. Each calculation used a $6 \times 6 \times 6$ supercell consisting of 216 atoms. Monkhorst-Pack [35] k-point meshes of $4 \times 4 \times 4$ and $8 \times 8 \times 8$ were used for vibrational and electronic supercell calculations, respectively.

We performed spin-polarized DFT calculations at 1000 K from initial paramagnetic, ferromagnetic, and antiferromagnetic spin configurations. Upon convergence, the magnetic polarizations in all cases were less than 0.08 μ_B on individual atoms and less than 0.05 μ_B in the orientational averages of spins. Calculations were performed for positive and negative dilations of the lattice, with no notable effect on the converged magnetic polarization. To balance computational cost with supercell size and complexity, non-spin-polarized calculations were used for the phonon dynamics.

1. Quasiharmonic

Phonon calculations within the quasiharmonic approximation were conducted with Phonopy [36]. A finite atomic displacement was introduced into each supercell of a grid of minimized 0 K supercells scaled by $\pm 0.5\%, \pm 1\%, \pm 1.5\%$ volume. Static calculations of each were converged to within 10^{-7} eV for accurate force constant determination. The harmonic approximation from $T = 0$–1500 K was applied to each volume, and a grid of these free energy curves was fitted to a Birch-Murnaghan equation of state. The minimized volumes at 330, 1000, and 1500 K were used to create corresponding dynamical matrices and predict phonon properties. A q-point mesh of $70 \times 70 \times 70$ was necessary for proper convergence, and the calculated phonon DOSs were convoluted with a Gaussian of 1.0 meV to approximate the broadening at higher phonon energies from the instrumental resolution. Lattice and thermodynamic properties calculated within this approximation depend on temperature only through a volume mapping, $\omega = \omega(V(T))$. More details on this process are provided in the Supplemental Material [25].

2. Anharmonic

Anharmonic contributions to thermodynamic properties were calculated using the stochastic temperature-dependent effective potential method (sTDEP) [37]. In this procedure, the Born-Oppenheimer surface of a material at a given temperature is represented using a collection of static calculations on supercells of thermally displaced atoms. These displacements were generated by a stochastic sampling of a

canonical ensemble at the temperature of interest. The energies, forces, and displacements of each configuration were tabulated and used to generate force constants with a least-squares fit to a model Hamiltonian,

$$\mathcal{H} = U_0 + \sum_i \frac{p_i^2}{2m_i} + \frac{1}{2!}\sum_{ij\alpha\beta} \Phi_{ij}^{\alpha\beta} u_i^\alpha u_j^\beta + \frac{1}{3!}\sum_{ijk\alpha\beta\gamma} \Phi_{ijk}^{\alpha\beta\gamma} u_i^\alpha u_j^\beta u_k^\gamma, \quad (3)$$

where $u_{\{i,j,k\}}$ is the displacement of atom $\{i, j, k\}$ and α, β, γ are the Cartesian components. The temperature-dependent U_0 is a fit parameter for the baseline of the potential energy surface. The sum containing Φ_{ij}, the quadratic force constants, captures some anharmonic and electron-phonon effects at a given temperature, and the final sum includes phonon-phonon interactions through the cubic force constants, Φ_{ijk}. The latter two terms in the model Hamiltonian are used to calculate anharmonic shifts and broadenings of phonon modes with respect to temperature. The force constants computed with this method include explicit temperature and volume dependencies.

A grid of 36 volumes and temperatures was created. For each point on the grid, an ensemble of ten supercells was generated with stochastically displaced atomic positions. DFT calculations were performed on each supercell to obtain energy-force-displacement data. The resulting energies were fitted to the Birch-Murnaghan equation of state to find the optimized volume for a given temperature. This volume and the calculated force constants were used to create another set of configurations on the temperature volume grid, and the minimization process was repeated. In this way, the force constants are numerically converged with respect to the number of configurations and supercell size. The final minimized free energies were utilized to calculate the equilibrium volume at each temperature, and phonon properties were evaluated at these conditions. Renormalization of phonon frequencies due to anharmonicity was included in these evaluations. Using phonon self-energy corrections from many-body theory [26,38], $\sum(\vec{\Omega}) = \Delta(\vec{\Omega}) + i\Gamma(\vec{\Omega})$, shifts and broadenings of the phonon DOS were calculated. Further details are provided in the Supplemental Material [25].

III. RESULTS

Phonon densities of states (DOSs) from TOF spectra of Cr are shown in Fig. 1. Shifts of the phonon DOSs from 6–1493 K follow the expected trend of "softening," or reduction of energy, with an increase in temperature. Interestingly, above 600 K, the three defined mode peaks (low transverse, T_2, high transverse, T_1, and longitudinal, L) appear as two peaks. This is traced to a large thermal softening of approximately 8 meV of the high-transverse mode between 6 and 1493 K.

Figure 2 shows the temperature dependence of the phonon dispersions between 6–1493 K, obtained by fitting the experimental DOSs to a BvK model [27]. We performed fits iteratively using a genetic algorithm optimization [39] (see Sec. II B). Along the $\Gamma \rightarrow H \rightarrow P \rightarrow \Gamma$ pathway, the trans-

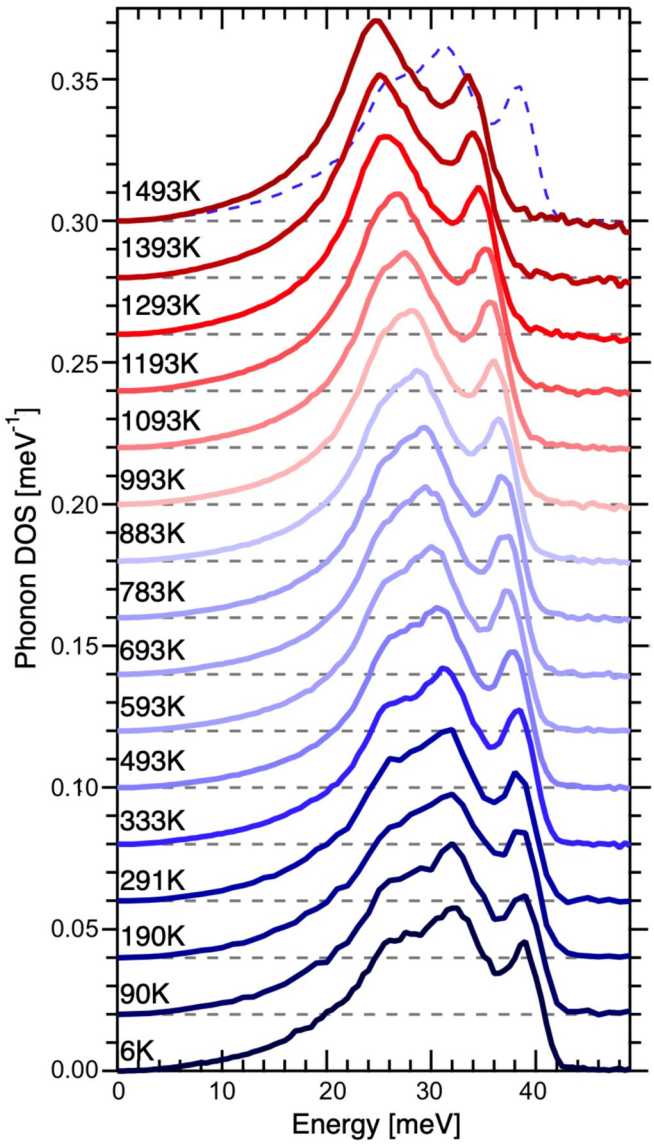

FIG. 1. Cr phonon DOSs from 6–149 K measured by TOF. Curves are offset for clarity, and the 333 K dataset is overlaid with the 1493 K curve to show the magnitude of the shift between 333 and 1493 K. Experimental error bars (based on counting statistics) are not shown because their height is approximately the width of the line used to connect data points.

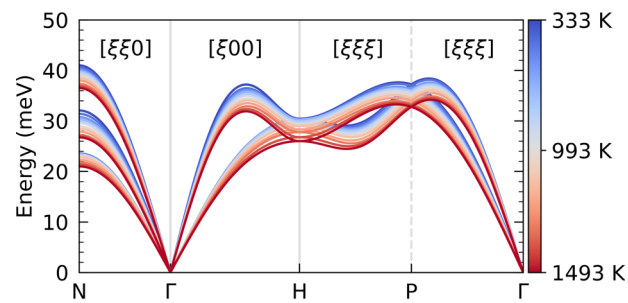

FIG. 2. Phonon dispersion relations from force constant optimization of BvK fits of the experimental phonon DOSs (333–1493 K). Two nearest neighbors (four variables) were considered in the fit.

verse modes are degenerate and exhibit a softening similar to the longitudinal mode. From N → Γ, there is a branch-dependent decrease in energy with respect to temperature. We illustrate these shifts relative to 330 K at each high-symmetry point in Fig. 3. The largest softening (of approximately 17%) occurs in the high-transverse mode between 330–1493 K. This behavior is consistent with the DOSs of Fig. 1.

Figure 4 shows the calculated and experimental DOSs at 330, 1000, and 1500 K. Colored bars representing mode peaks fitted to three Lorentzians show the average shift of each feature. Densities of states calculated with sTDEP show similar peak location, shape, and softening to the experimental spectra at 330 and 1500 K. Our quasiharmonic predictions do not accurately reproduce the features in the DOS at these temperatures, indicating that anharmonicity is important for the thermal trends of phonons in Cr.

Our experimental and calculated phonon dispersions at 330, 1000, and 1500 K are plotted in Fig. 5. Quasiharmonic and anharmonic calculations agree well with experimental data along most of the high-symmetry reciprocal space pathways. A notable exception is the N → Γ direction, where the QH low-transverse modes show an anomaly at the N point, and the high-transverse modes do not shift as strongly as expected. The AH and QH calculations also give different magnitudes of the longitudinal mode along the Γ → H path.

A way to assess the thermodynamic consequences of anharmonic phonon behavior is by calculating entropy. Figure 6 shows the electronic, vibrational, and electron-phonon components of entropy and their respective contributions to the total entropy as determined by JANAF [18].

The calculated lattice expansions are compared to experimental results in Fig. 7. Both QH and sTDEP *ab initio* calculations are in agreement with lattice parameters obtained from the elastic region of our neutron scattering measurements, and with previous experimental results that are labeled in the figure.

IV. DISCUSSION

A. Phonons

The experimental phonon DOSs of bcc Cr show significant softening at elevated temperatures, and the apparent disappearance of one of the Van Hove singularities in Fig. 1 is a result of this temperature dependence. Phonon dispersions calculated with fitted force constants show that the largest softening occurs in the high-transverse mode. At the high-symmetry points, Γ, H, and P, the two transverse branches are degenerate. At the N point near 1000 K, Fig. 3 shows a softening of the high-transverse (T_1) mode and little softening of the low-transverse (T_2) mode. The shift of the high-transverse mode from ∼32 to ∼27 meV confirms that features in the phonon DOS with the largest thermal softening are associated with the $T_1[\xi, \xi, 0]$ phonon branch. At the N point, this T_1 mode involves the opposing displacements of two neighboring (110) planes along the $[1\bar{1}0]$ direction [40]. The relatively small thermal softening of the low-transverse mode, $T_2[\xi, \xi, 0]$, up to 1000 K also may originate from interactions beyond the harmonic approximation.

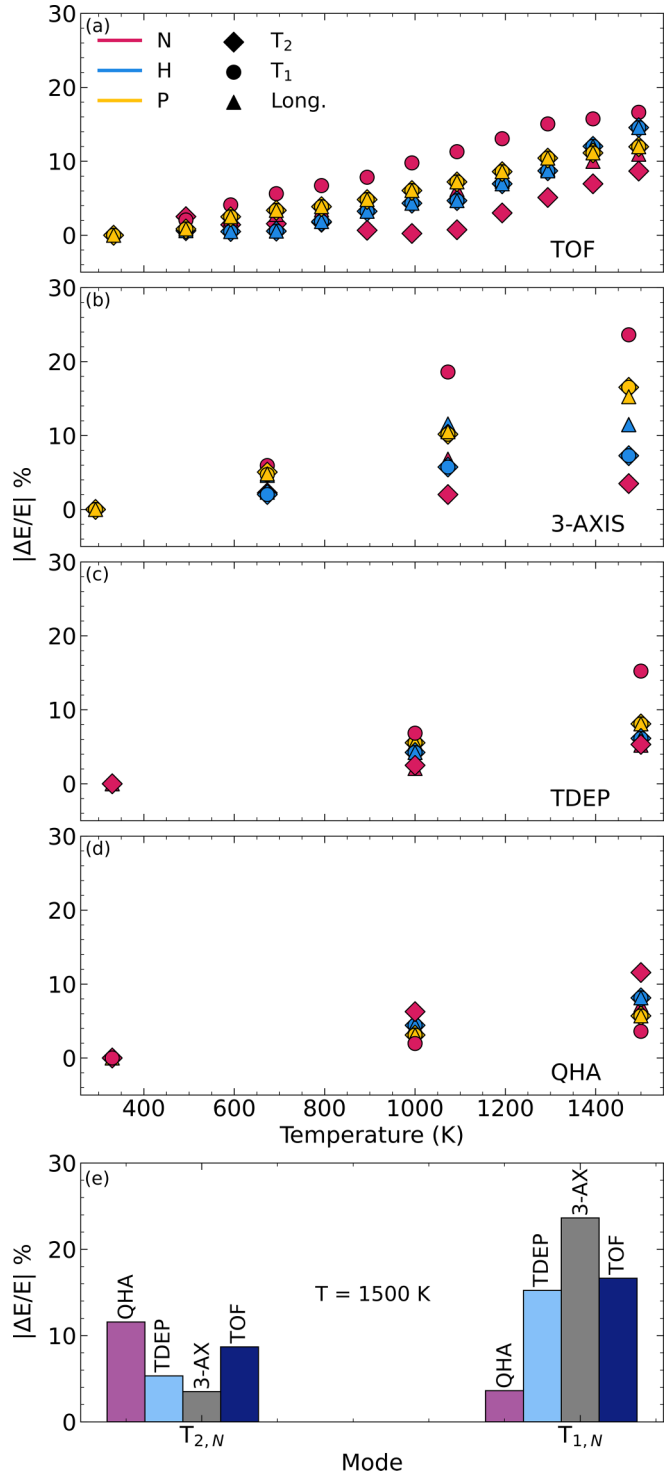

FIG. 3. Thermal shifts, relative to ambient temperature, of the phonons in Cr at each non-Γ high-symmetry point for (a) our TOF measurements, (b) previous triple-axis experiments [40], (c) AH calculations, and (d) QH calculations. A comparison of the thermal shifts for each method at 1500 K for the T_1 and T_2 modes at the N point is shown in (e).

At 330 K, the high-transverse and longitudinal modes in the DOS have higher energies in the QH calculations than from TOF measurements and anharmonic sTDEP calculations. This overestimation of peak locations continues to

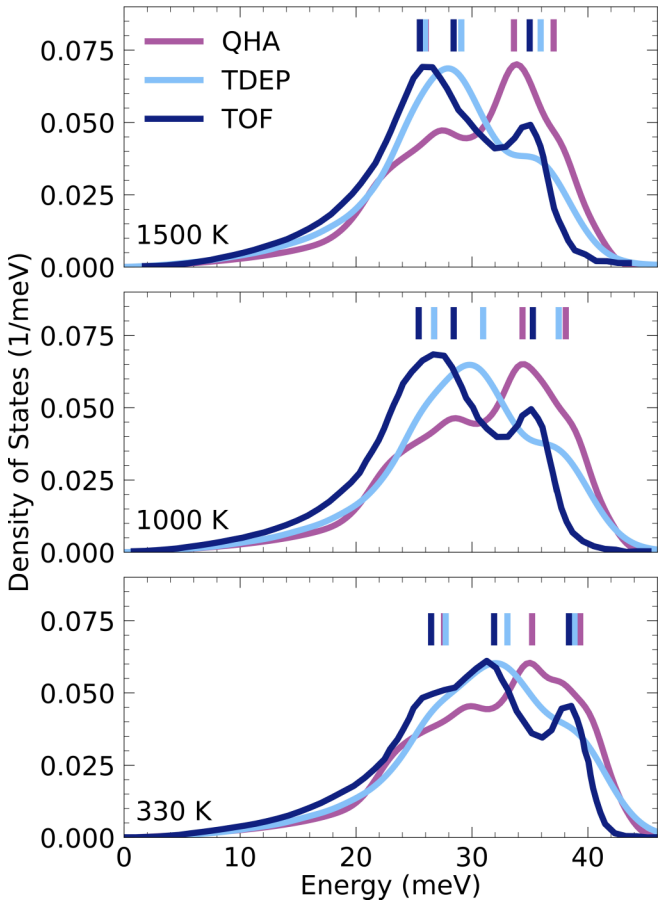

FIG. 4. Phonon densities of states at 330 (bottom), 1000 (middle), and 1500 K (top). Each panel compares the experimental phonon DOS (dark blue) to the calculated DOSs from quasiharmonic (purple) and anharmonic (light blue) approximations. The colored markers indicate peak locations from a Lorentzian fit to the features of the DOSs.

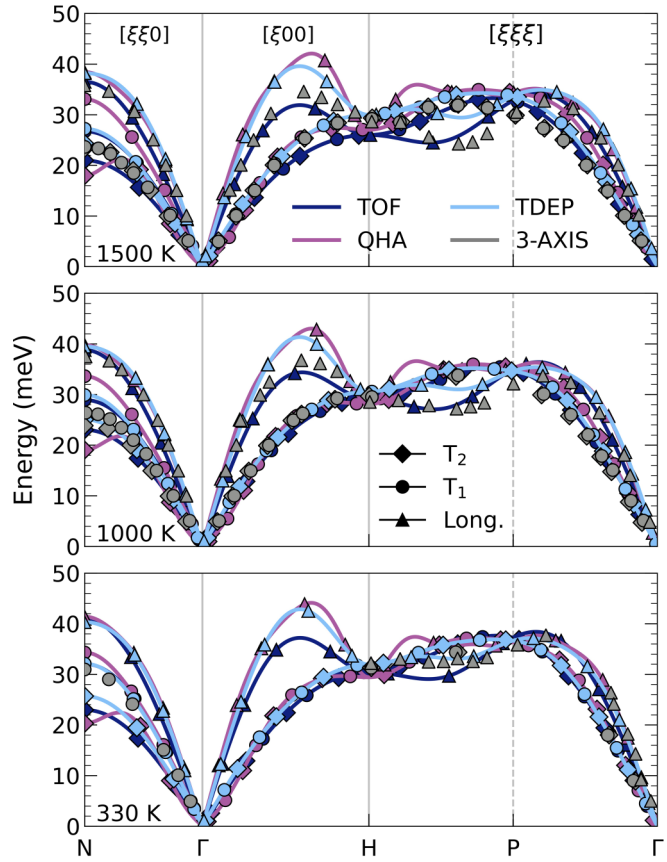

FIG. 5. Comparison of experimental and calculated phonon dispersion relations at 330 K (bottom), 1000 K (middle), and 1500 K (top). Symbols to distinguish the low transverse (diamonds), high transverse (circles), and longitudinal (triangles) phonon branches are also shown. Anharmonic (light blue) and quasiharmonic (purple) dispersions are in good agreement with a BvK fit to experimental data (dark blue) and existing triple-axis data (gray) [40]. The anharmonic calculations capture behavior along the H to P high-symmetry path better than the quasiharmonic simulations.

1500 K. Consequently, the shape of the DOS is skewed in the QH approximation, with more features appearing at higher energies than those found with measurements and sTDEP calculations. The agreement of the DOS calculated with the AH approximation and TOF measurements is excellent at 330 and 1500 K, despite some excessive broadening of the longitudinal Van Hove singularity.

There is a general agreement of phonon dispersions calculated with each model and experimental data at 330, 1000, and 1500 K along $\Gamma \rightarrow H \rightarrow P \rightarrow \Gamma$ (Fig. 5). However, the QH approximation inverts the energies of the T_1 and T_2 modes at the N point. This is accentuated by the anomaly in the low-transverse branch behavior at N in the QH dispersions. This discrepancy is better seen with Fig. 3(e). In the QH approximation, the low-transverse branch shows the largest thermal softening at N. This disagrees with the general trend seen in the experimental data and AH calculations: the high-transverse phonon branch has the larger thermal softening. Quasiharmonic models sometimes predict accurate macroscopic properties without capturing the underlying phonon physics [43,44].

We attribute the failure of the QH approximation in Cr to the underlying assumption of noninteracting phonons. This assumption is known to fail at higher temperatures, where temperature-dependent phonon-phonon interactions begin to dominate [1,45–47]. The QH model cannot capture these effects because the frequencies within this model, $\omega = \omega(V(T))$, incorporate temperature by shifting harmonic frequencies with changes in volume. This approach ignores terms beyond the quadratic phonon self-energy, which are needed for lifetime broadening and purely temperature-dependent (AH) shifts. Our sTDEP calculations include cubic order corrections of the phonon self-energy, so $\omega = \omega(V, T)$.

The QH approximation did not successfully predict the thermal softenings of individual phonons, but there is reasonable agreement between the vibrational entropy calculated with QH and AH methods. The change in phonon frequency at the N point gives insight into why. Summing the fractional thermal shifts ($T_1 + T_2 + L$) from the QH calculations at the N zone boundary gives a change of about 22%. A similar sum for our AH calculations gives a change of 26%, which is

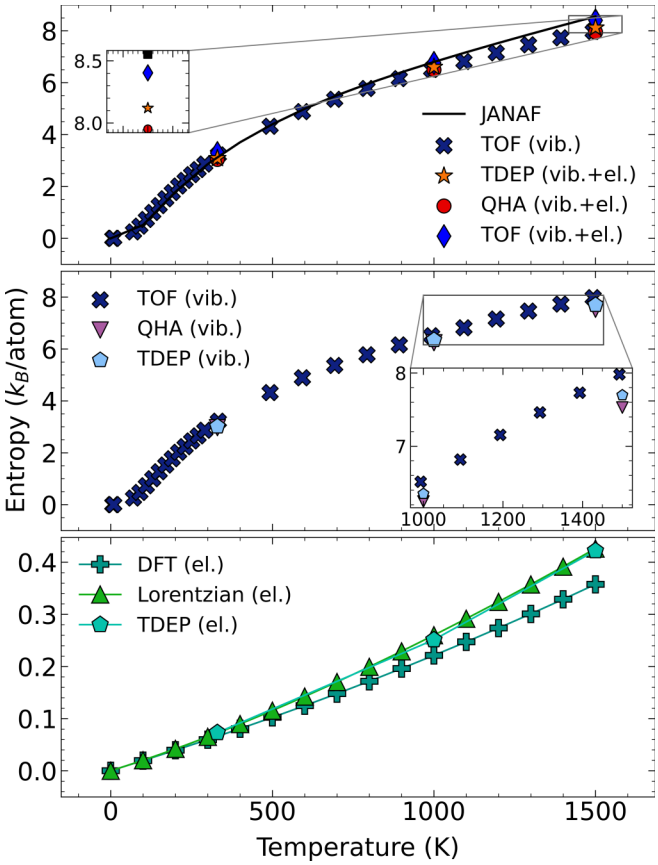

FIG. 6. Components of entropy compared to the total JANAF entropy [18]. (Bottom) Electronic entropy including temperature-dependent electron-phonon coupling. (Middle) Vibrational entropy calculated from DOSs using TOF INS, a quasiharmonic approximation, and an anharmonic approximation. (Top) Sum of the electronic and vibrational components of entropy from experiment and computations versus the calorimetric total entropy.

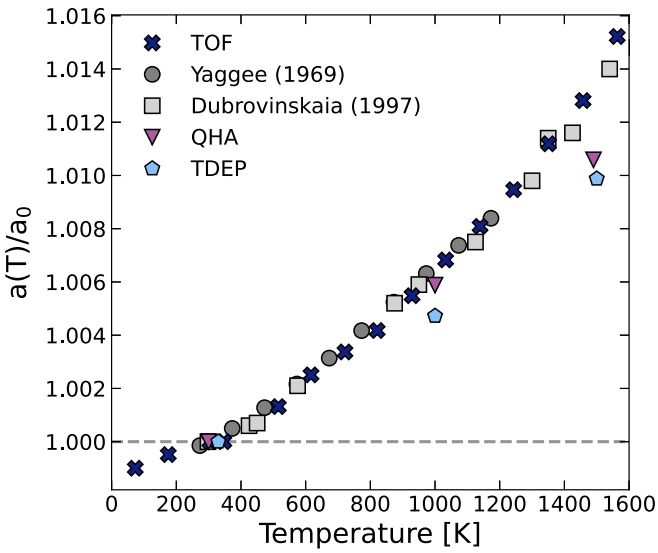

FIG. 7. Lattice expansion of Cr from 6–1500 K with respect to ambient temperature. Previous lattice expansions are reproduced from [41,42].

comparable. This shows some cancellation of errors in the average behavior of phonon branches from the QH calculations, giving them better success with the vibrational entropy.

Likewise, a good prediction of thermal expansion does not validate the QH approximation for predictions of phonon physics. Using

$$\frac{\partial^2 F}{\partial V \partial T} = -\beta B_T \tag{4}$$

and $F(V,T) = U(V,T) - TS(V,T)$, it is evident that thermal expansion, β, and bulk modulus, B_T, are explicitly dependent on both volume and temperature. Any cancellation of errors introduced in calculated entropy will be present in predictions of thermal expansion (and bulk modulus). It is therefore plausible that the QH approximation can successfully reproduce the thermal expansion of Cr (Fig. 7), even with the wrong thermal trends of individual phonons.

There is an underestimation of 4% in the sTDEP vibrational entropy at 1500 K, illustrated in the middle panel of Fig. 6. This is caused by an overbinding in the generalized gradient approximation (GGA) for Cr [48], which also affects our ground state lattice parameter ($a = 2.845$ Å). This is consistent with the ∼4% average overstiffening of the phonon dispersions (Fig. 5), and the slight underestimation of the lattice expansion (Fig. 7). A similar effect occurs in our QH calculations.

B. Entropy and free energy

The top panel in Fig. 6 shows that for temperatures up to 600 K, the phonon entropy from TOF INS experiments accounts for nearly all of the total entropy [18]. At 1500 K, the S_{vib} from TOF measurements or calculations accounts for over 89% of the total entropy of Cr. The remainder originates primarily from the occupancy of electronic states, the change of these states with temperature, and perhaps magnetic entropy [15,17].

Figure 6 shows that an electronic entropy S_{ele}, calculated first by including the temperature dependence of the electronic entropy through the Fermi-Dirac distribution with the ground state electronic states, brings the sum of entropies S_{tot} closer to the JANAF thermodynamic data, where

$$S_{\text{tot}} = S_{\text{vib}} + S_{\text{ele}} + S_{\text{mag}}. \tag{5}$$

Thermal motions of atoms broaden the electronic states through electron-phonon interactions. This temperature dependence was calculated with supercells consisting of thermally displaced atoms obtained by sTDEP at 330, 1000, and 1500 K, and is shown in Fig. 6. The electronic entropy was also calculated by the simpler process following Thiessen [49] and Grimvall [50], where the ground state electronic DOS, $\rho_{\text{gnd}}(E)$, is convoluted with a function of Lorentzian form

$$\rho(E) = \rho_{\text{gnd}}(E) * \mathcal{L}(2\Gamma), \tag{6}$$

to approximate the effects of electron-phonon interactions on electronic DOS, $\rho(E)$. The amount of broadening, $2\Gamma = 2\pi\lambda k_B T$, used a value of $\lambda = 0.5$ [51]. Figure 6 shows very good agreement between these two approaches.

Adding the thermally broadened S_{ele} to the experimental and computational S_{vib} gives our best estimates of the total

entropy of bcc chromium. Figure 6 shows that the sum of the measured TOF vibrational and electronic components gives excellent agreement with the JANAF data from calorimetric measurements. There is, however, something missing from the anharmonic phonon calculations, as seen by the inset at the top of Fig. 6. A similar discrepancy was found in previous anharmonic calculations [17], which proposed that the extra entropy required for agreement with calorimetry was magnetic in origin. However, the experimental phonon entropy is larger than these anharmonic calculations, and with the electronic entropy, the total entropy agrees well with calorimetry. The discrepancy is in the anharmonic calculations of the phonon DOS, which are stiffer and give a lower phonon entropy than the measurements. The additional nonharmonic contribution to the phonon self-energy is unexplained, but an effect from phonon-paramagnon interactions could be a candidate. Paramagnon energies were calculated recently by time-dependent density functional theory at 0 K [52]. These energies were found to be large, and may not change strongly with temperature. Showing the effects of paramagnons on phonon energies at high temperatures may require new computations. Nevertheless, a large, explicit contribution from magnetic entropy is not needed to account for the thermodynamic entropy of Cr at high temperatures.

V. CONCLUSIONS

The phonon DOS was measured on bcc chromium from 6 to 1493 K by TOF INS, and calculations of the phonons were performed with QH and AH approximations using Phonopy and sTDEP. To obtain detail on individual phonon branches, the experimental DOSs were fitted to a Born–von Kármán model using force constants adjusted with a global minimizer. Both measurements and computations showed significant thermal softening of the phonons, and a similar average phonon softening. However, the QH approximation predicted that the low-transverse branch would soften faster than the high-transverse branch, whereas the opposite trend is found by AH sTDEP calculations, and by TOF results from the present work and a previous study. The thermodynamic entropy of chromium was obtained from the experimental phonon DOS, and the electronic entropy from *ab initio* calculations. Their sum gave an entropy for chromium that was in excellent agreement with JANAF results obtained by assessing calorimetric data. An explicit magnetic entropy contribution is not needed for temperatures above 330 K, but a paramagnon susceptibility may perturb phonon energies beyond the known effects of quasiharmonic, anharmonic, and electron-phonon interactions.

ACKNOWLEDGMENTS

We thank Jiao Y. Y. Lin for his discussions and assistance with MCViNE modeling. This research used resources at the Spallation Neutron Source, a DOE Office of Science User Facility operated by the Oak Ridge National Laboratory. This work used resources from National Energy Research Scientific Computing Center (NERSC), a DOE Office of Science User Facility supported by the Office of Science of the U.S. Department of Energy under Contract No. DE-AC02-05CH11231. This work was supported by the DOE Office of Science, BES, under Contract No. DE-FG02-03ER46055.

[1] B. Fultz, Prog. Mater. Sci. **55**, 247 (2010).
[2] D. Lamago, M. Hoesch, M. Krisch, R. Heid, K.-P. Bohnen, P. Böni, and D. Reznik, Phys. Rev. B **82**, 195121 (2010).
[3] N. Shulumba, B. Alling, O. Hellman, E. Mozafari, P. Steneteg, M. Odén, and I. A. Abrikosov, Phys. Rev. B **89**, 174108 (2014).
[4] A. R. Natarajan, P. Dolin, and A. Van der Ven, Acta Mater. **200**, 171 (2020).
[5] L. Hao, A. Ruban, and W. Xiong, Calphad **73**, 102268 (2021).
[6] M. Heine, O. Hellman, and D. Broido, Phys. Rev. B **103**, 184409 (2021).
[7] S. Anzellini, D. Errandonea, L. Burakovsky, J. E. Proctor, R. Turnbull, and C. M. Beavers, Sci. Rep. **12**, 6727 (2022).
[8] O. Eriksson, J. M. Wills, and D. Wallace, Phys. Rev. B **46**, 5221 (1992).
[9] L. Néel, Ann. Phys. (Paris) **11**, 232 (1936).
[10] M. K. Wilkinson, E. O. Wollan, W. C. Koehler, and J. W. Cable, Phys. Rev. **127**, 2080 (1962).
[11] B. H. Grier, G. Shirane, and S. A. Werner, Phys. Rev. B **31**, 2892 (1985).
[12] K. Thurnay, *Thermal Properties of Transition Metals* (Forschungszentrum, Karlsruhe, 1998).
[13] C. Y. Young and J. B. Sokoloff, J. Phys. F: Met. Phys. **4**, 1304 (1974).
[14] J. O. Andersson, Int. J.Thermophys. **6**, 411 (1985).
[15] G. Grimvall, J. Häglund, and A. Fernández Guillermet, Phys. Rev. B **47**, 15338 (1993).
[16] W. Xiong, M. Selleby, Q. Chen, J. Odqvist, and Y. Du, Crit. Rev. Solid State Mater. Sci. **35**, 125 (2010).
[17] F. Körmann, B. Grabowski, P. Söderlind, M. Palumbo, S. G. Fries, T. Hickel, and J. Neugebauer, J. Phys.: Condens. Matter **25**, 425401 (2013).
[18] M. Chase, *NIST-JANAF Thermochemical Tables, 4th Edition* (American Institute of Physics, -1, 1998).
[19] A. Obaied, B. Bocklund, S. Zomorodpoosh, L. Zhang, R. Otis, Z.-K. Liu, and I. Roslyakova, Calphad **69**, 101762 (2020).
[20] D. L. Abernathy, M. B. Stone, M. J. Loguillo, M. S. Lucas, O. Delaire, X. Tang, J. Y. Y. Lin, and B. Fultz, Rev. Sci. Instrum. **83**, 015114 (2012).
[21] J. L. Niedziela, R. Mills, M. J. Loguillo, H. D. Skorpenske, D. Armitage, H. L. Smith, J. Y. Y. Lin, M. S. Lucas, M. B. Stone, and D. L. Abernathy, Rev. Sci. Instrum. **88**, 105116 (2017).
[22] O. Arnold, J. C. Bilheux, J. M. Borreguero, A. Buts, S. I. Campbell, L. Chapon, M. Doucet, N. Draper, R. Ferraz Leal, M. A. Gigg, V. E. Lynch, A. Markvardsen, D. J. Mikkelson, R. L. Mikkelson, R. Miller, K. Palmen, P. Parker, G. Passos, T. G. Perring, P. F. Peterson *et al.*, Nucl. Instrum. Methods Phys. Res. Sect. A **764**, 156 (2014).
[23] J. Y. Y. Lin, F. Islam, and M. Kresh, J. Open Source Sof. **3**, 440 (2018).

[24] J. Y. Y. Lin, H. L. Smith, G. E. Granroth, D. L. Abernathy, M. D. Lumsden, B. Winn, A. A. Aczel, M. Aivazis, and B. Fultz, Nucl. Instrum. Methods Phys. Res. Sect. A **810**, 86 (2016).
[25] See Supplemental Material at http://link.aps.org/supplemental/10.1103/PhysRevB.107.054312 for more information on experimental design, computational modeling, fitting methods, and corrections for sample curvature.
[26] D. C. Wallace, *Thermodynamics of Crystals*, Dover Books on Physics (Dover Publications, 1998).
[27] L. Mauger, M. S. Lucas, J. A. Muñoz, S. J. Tracy, M. Kresch, Y. Xiao, P. Chow, and B. Fultz, Phys. Rev. B **90**, 064303 (2014).
[28] G. Kresse and J. Hafner, Phys. Rev. B **47**, 558 (1993).
[29] G. Kresse and J. Hafner, Phys. Rev. B **49**, 14251 (1994).
[30] G. Kresse and J. Furthmüller, Phys. Rev. B **54**, 11169 (1996).
[31] G. Kresse and D. Joubert, Phys. Rev. B **59**, 1758 (1999).
[32] P. E. Blöchl, Phys. Rev. B **50**, 17953 (1994).
[33] J. P. Perdew, K. Burke, and M. Ernzerhof, Phys. Rev. Lett. **77**, 3865 (1996).
[34] J. P. Perdew, K. Burke, and M. Ernzerhof, Phys. Rev. Lett. **78**, 1396(E) (1997).
[35] H. J. Monkhorst and J. D. Pack, Phys. Rev. B **13**, 5188 (1976).
[36] A. Togo and I. Tanaka, Scr. Mater. **108**, 1 (2015).
[37] O. Hellman, I. A. Abrikosov, and S. I. Simak, Phys. Rev. B **84**, 180301(R) (2011).
[38] A. A. Maradudin, A. E. Fein, and G. H. Vineyard, Phys. Status Solidi B **2**, 1479 (1962).
[39] L. M. Mauger, Phonon thermodynamics of iron and cementite, Ph.D. thesis, California Institute of Technology, 2015.
[40] J. Trampenau, W. Petry, and C. Herzig, Phys. Rev. B **47**, 3132 (1993).
[41] F. L. Yaggee, E. R. Gilbert, and J. W. Styles, J. Less-Common Met. **19**, 39 (1969).
[42] N. A. Dubrovinskaia, L. S. Dubrovinsky, S. K. Saxena, and B. Sundman, Calphad **21**, 497 (1997).
[43] D. S. Kim, H. L. Smith, J. L. Niedziela, C. W. Li, D. L. Abernathy, and B. Fultz, Phys. Rev. B **91**, 014307 (2015).
[44] C. N. Saunders, D. S. Kim, O. Hellman, H. L. Smith, N. J. Weadock, S. T. Omelchenko, G. E. Granroth, C. M. Bernal-Choban, S. H. Lohaus, D. L. Abernathy, and B. Fultz, Phys. Rev. B **105**, 174308 (2022).
[45] Y. Shen, C. N. Saunders, C. M. Bernal, D. L. Abernathy, M. E. Manley, and B. Fultz, Phys. Rev. Lett. **125**, 085504 (2020).
[46] T. Lanigan-Atkins, S. Yang, J. L. Niedziela, D. Bansal, A. F. May, A. A. Puretzky, J. Y. Y. Lin, D. M. Pajerowski, T. Hong, S. Chi, G. Ehlers, and O. Delaire, Nat. Commun. **11**, 4430 (2020).
[47] F. Knoop, T. A. R. Purcell, M. Scheffler, and C. Carbogno, Phys. Rev. Mater. **4**, 083809 (2020).
[48] R. Hafner, D. Spišák, R. Lorenz, and J. Hafner, Phys. Rev. B **65**, 184432 (2002).
[49] M. Thiessen, Int. J. Thermophys. **7**, 1183 (1986).
[50] G. Grimvall, *Thermophysical Properties of Materials* (Elsevier, Amsterdam, 2008).
[51] G. Grimvall, *The Electron-Phonon Interaction in Metals* (North-Holland, New York, 1981).
[52] K. Cao, H. Lambert, P. G. Radaelli, and F. Giustino, Phys. Rev. B **97**, 024420 (2018).